Acta Pharmaceutica Sinica B 2022;12(1):424–436

Chinese Pharmaceutical Association
Institute of Materia Medica, Chinese Academy of Medical Sciences

Acta Pharmaceutica Sinica B

www.elsevier.com/locate/apsb
www.sciencedirect.com

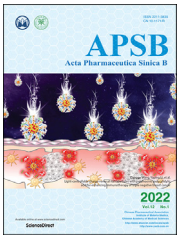

ORIGINAL ARTICLE

GSH-sensitive polymeric prodrug: Synthesis and loading with photosensitizers as nanoscale chemo-photodynamic anti-cancer nanomedicine

Lei Luo[b], Yiming Qi[b], Hong Zhong[b], Shinan Jiang[b], Hu Zhang[d], Hao Cai[a], Yahui Wu[a], Zhongwei Gu[a], Qiyong Gong[a,c], Kui Luo[a,*]

[a]*Huaxi MR Research Center (HMRRC), Department of Radiology, Functional and Molecular Imaging Key Laboratory of Sichuan Province, National Clinical Research Center for Geriatrics, West China Hospital, Sichuan University, Chengdu 610041, China*
[b]*College of Pharmaceutical Sciences, Southwest University, Chongqing 400716, China*
[c]*Research Unit of Psychoradiology, Chinese Academy of Medical Sciences, Chengdu 610041, China*
[d]*Amgen Bioprocessing Centre, Keck Graduate Institute, Claremont, CA 91711, USA*

Received 24 February 2021; received in revised form 23 March 2021; accepted 30 March 2021

KEY WORDS

Stimuli responsiveness;
Polymeric prodrug;
Photodynamic therapy;
Combinational therapy;
Nanomedicine

Abstract Precisely delivering combinational therapeutic agents has become a crucial challenge for anti-tumor treatment. In this study, a novel redox-responsive polymeric prodrug (molecular weight, MW: 93.5 kDa) was produced by reversible addition–fragmentation chain transfer (RAFT) polymerization. The amphiphilic block polymer-doxorubicin (DOX) prodrug was employed to deliver a hydrophobic photosensitizer (PS), chlorin e6 (Ce6), and the as-prepared nanoscale system [NPs(Ce6)] was investigated as a chemo-photodynamic anti-cancer agent. The glutathione (GSH)-cleavable disulfide bond was inserted into the backbone of the polymer for biodegradation inside tumor cells, and DOX conjugated onto the polymer with a disulfide bond was successfully released intracellularly. NPs(Ce6) released DOX and Ce6 with their original molecular structures and degraded into segments with low MWs of 41.2 kDa in the presence of GSH. NPs(Ce6) showed a chemo-photodynamic therapeutic effect to kill 4T1 murine breast cancer cells, which was confirmed from a collapsed cell morphology, a lifted level in the intracellular reactive oxygen species, a reduced viability and induced apoptosis. Moreover, *ex vivo* fluorescence images indicated that NPs(Ce6) retained in the tumor, and exhibited a remarkable *in vivo* anticancer efficacy. The combinational therapy showed a significantly increased tumor growth inhibition (TGI, 58.53%). Therefore, the redox-responsive, amphiphilic block polymeric prodrug could have a great potential as a chemo-photodynamic anti-cancer agent.

*Corresponding author. Tel./fax: +86 28 85422538.
E-mail address: luokui@scu.edu.cn (Kui Luo).

Peer review under responsibility of Chinese Pharmaceutical Association and Institute of Materia Medica, Chinese Academy of Medical Sciences.

https://doi.org/10.1016/j.apsb.2021.05.003

1. Introduction

Chemotherapy is generally considered to be one of the most efficient methods for antitumor therapy, while photodynamic therapy (PDT), which uses light to excite photosensitizers (PSs) to generate reactive oxygen species (ROS) for oxidizing intracellular biomacromolecules to induce the death of tumor cells, offers minimal invasive treatment for assisting in chemotherapy[1,2]. However, a low antitumor efficiency and severe systemic toxic effects of chemotherapeutics and poor water solubility and insufficient tumor accumulation of PDT agents have hampered their application[3]. To overcome these challenges, nanomedicines derived from liposomes, micelles, nanoparticles, dendrimers and other polymers have been applied as drug delivery systems (DDSs) for anti-tumor agents[4−10]. These nanomedicines have improved their accumulation owing to the enhanced permeability and retention (EPR) effect, which can decrease side effects and enhance therapeutic efficacies[11−14]. Among these reported systems, functional polymers in response to the tumor microenvironment have been designed as smart DDSs with great potential for cancer diagnosis and therapy.

Some of DDSs are designed in such a way that their structures can be disrupted to release the encapsulated cargo upon triggering by changes in the intensity of the stimuli after they enter the microenvironment at the tumor tissue (*e.g.*, pH, temperature and redox potential)[15−21]. However, to achieve high drug retention from DDSs at tumor sites and rapid drug release intracellularly remains challenging. A new strategy of preparing a polymer−drug conjugate as a ′prodrug′ has attracted extensive attention. Polymers and drugs are conjugated *via* a microenvironmental stimuli-responsive linker with many advantages, such as modifiable structures, increased water solubility, prolonged circulation in the blood, enhanced distribution in tumor tissues and stimuli-responsive drug release inside tumor cells[22−25].

The success of polymeric drug delivery depends on polymeric carriers, including their compositions, structures and molecular weights[26]. Only a few polymer-based conjugates have entered into clinical applications and trials, including poly[*N*-(2-hydroxypropyl) methacrylamide] (polyHPMA)[27−29]. Recently, studies have shown that a long blood circulation time and a high targeting efficiency can be achieved *via* increasing molecular weights of polyHPMA-drug prodrugs. Conjugates with high molecular weights prepared from drugs with polyHPMA functionalized with a cathepsin B-responsive oligopeptide sequence, glycylphenylalanylleucylglycine (GFLG), have shown enhanced anticancer therapeutic indexes and great biosafety[26,30]. Our previous studies also demonstrate that highly stable nanoscale systems or nanoparticles can be obtained *via* optimization of structures of polyHPMA-drug prodrugs by replacing homopolymers with block and amphiphilic polymers[15,31,32]. The amphiphilic stimuli-responsive polyHPMA-drug prodrugs form nano-sized vehicles in an aqueous solution and these vehicles may be applied either as pro-drugs or carriers to deliver other agents for synergistic antitumor therapy.

The combination of two therapies has resulted in enhanced cancer therapeutic indexes after optimization. Recently, the strategy of combining chemotherapy with PDT has been reported with great promise[33−41]. Both chemotherapeutic drugs and photosensitizers (PSs) are loaded into one carrier and the co-delivery system can enhance the anticancer efficacy. Inorganic nanoparticles, dendrimers and polymers have been designed by using this strategy. In our previous report[42], we have prepared a cathepsin B/pH-sensitive drug−polymer conjugate and showed a decent efficacy against lung metastasis of breast cancer. However, for most reported polyHPMA-drug prodrugs, drugs including DOX are conjugated to carriers *via* the tetrapeptide GFLG linker. The anticancer efficacy remains dissatisfactory, which may be due to high steric hindrance of the moiety of GFLG-DOX to the active site of the enzyme cathepsin B, resulting in a slow drug release rate in a tumor environment[43,44]. Therefore, we hypothesized after DOX is conjugated to polyHPMA with a low hindrance disulfide bond, the block and amphiphilic prodrug could be used as micelles to load other agents for better combinational therapy.

In this study, we prepared a disulfide bond-bridged polyHPMA-DOX polymeric prodrug (polyHPMA-DOX) which self-assembled into stimuli-responsive nanoparticles, and the prodrug was used to encapsulate Ce6, a PS from the porphyrin family. The proposed combined chemo-photodynamic therapy using this prodrug against breast cancer was illustrated in Fig. 1. The nanoparticles accumulated at the tumor site preferably *via* the EPR effect. Intracellular reductive GSH reacted with the prodrug nanoparticles to release DOX inside tumor cells since GSH is much higher in many tumor cells than that in normal cells. The released DOX combined with ROS generated from PDT interactively inhibited the growth of 4T1 murine breast cancer cells. A remarkable *in vivo* antitumor efficacy from the combination of chemotherapy and PDT was confirmed in BALB/c mice bearing 4T1 murine breast tumors. These results demonstrated that the polymeric prodrug loaded with Ce6 could act as high efficacious nanomedicines for breast cancer treatment.

2. Materials and methods

Materials and methods used for preparation of disulfide-functionalized monomers with DOX (MA-SS-DOX) and disulfide-functionalized chain transfer agents (CTA-SS-CTA) (Supporting Information Scheme S1), preparation of drug-loaded NPs(Ce6), CMC determination, drug release and degradation, cell culture and animal models, and structural characterizations were supplied in the Supporting Information (SI).

2.1. Synthesis of the polymeric prodrug via RAFT polymerization

HPMA (2.15 g, 15 mmol) and the functionalized CTA (CTA-SS-CTA, 8.5 mg, 12.6 μmol) were added to a vial, and the vial was

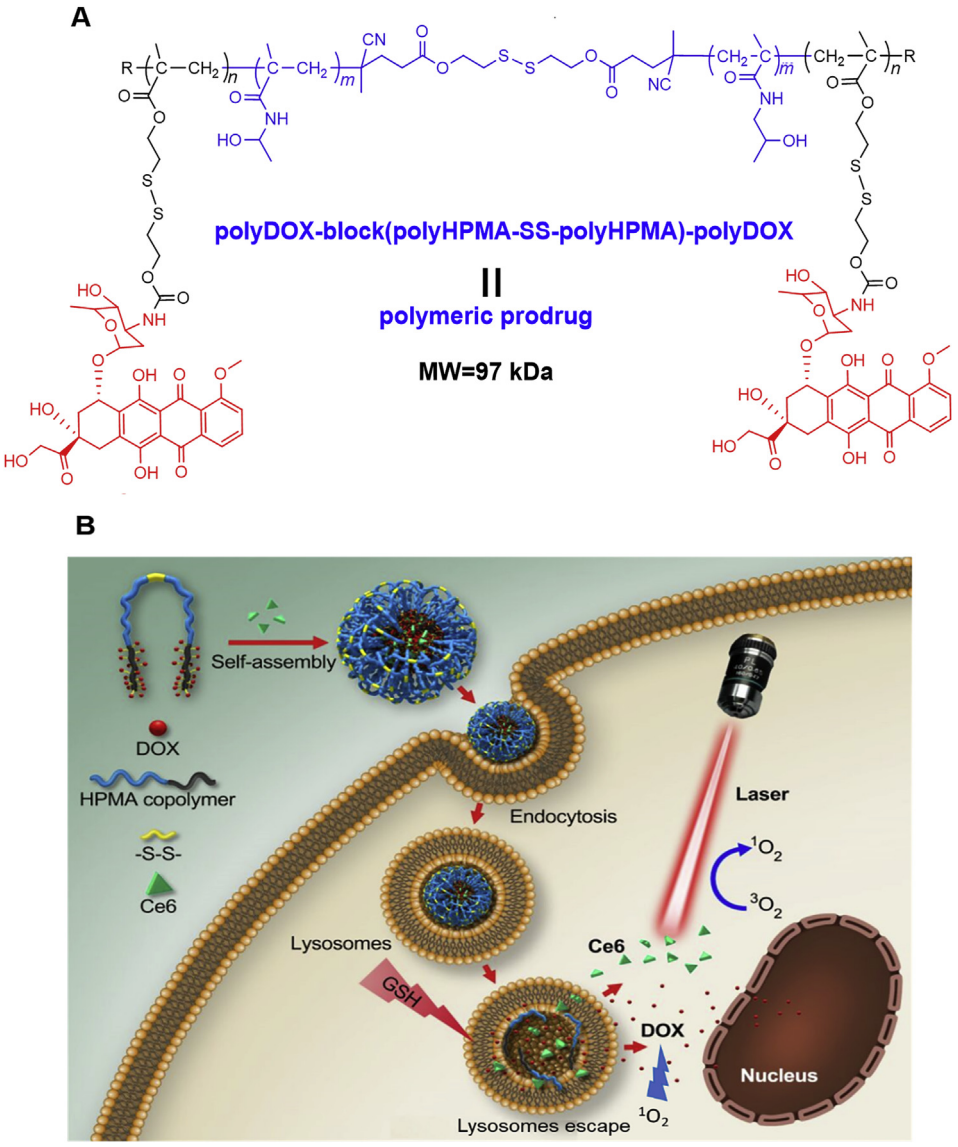

Figure 1 (A) The structure of the polymeric prodrug [polyDOX-*block*-(polyHPMA-SS-polyHPMA)-*block*-polyDOX] could be cleaved to low-molecular-weight segments to release the drug. (B) Illustration of cellular uptake of prodrug-based nanoparticles loaded with Ce6, drug release from nanoparticles, degradation of the polymeric backbone and synergistic antitumor therapy by combining Ce6-based PDT and DOX-based chemotherapy.

closed. A solution of water/methanol (6: 1, 10 mL) with VA-044 (2.7 mg, 8.4 μmol) was injected into the vial. Nitrogen was used to purge the solution for 50 min. The solution was stirred at 45 °C for 8 h. After stirring at 0 °C for 10 min, the vial was opened. The polymer was purified by precipitation in acetone three times, dried, giving 1.85 g slight pink powder (polyHPMA-SS-polyHPMA).

The polymer polyHPMA-SS-polyHPMA (1.53 g) and the functionalized monomer (MA-SS-DOX, 801 mg, 1.01 mmol) were added to a vial. A solution of water/DMSO (1: 2, total 7 mL) containing VA-044 (2.0 mg, 6.2 μmol) was added, and the solution was deoxygenated as above. Polymerization reaction proceeded at 44 °C for 24 h. The reaction solution was first purified *via* dialysis against water, and was further applied to a size exclusion chromatography column by using Superose 6 HR10/30, as shown in SI, giving red powder (polyDOX-block-(polyHPMA-SS-polyHPMA)-block-polyDOX, 1.51 g). The drug DOX content was measured *via* UV–Vis analysis to be 8.9% (*w*/*w*), as shown in Supporting Information Table S1.

2.2. *Determination of single oxygen ($^1O_2$)*

We evaluated the abilities of NPs(Ce6) to generate $^1O_2$ by using ADPA as an acceptor of $^1O_2$. Since the absorbance at 400 nm of ADPA was reduced after it was bleached in the presence of $^1O_2$, the change in the absorbance of ADPA provided a means of monitoring $^1O_2$ production from NPs(Ce6). The NPs(Ce6) sample (Ce6 5×10^{-6} mol/L, DOX 1.34×10^{-5} mol/L) was dissolved in the solution of PBS (pH = 7.4) with 2×10^{-5} mol/L ADPA and another 2×10^{-5} mol/L of ADPA without NPs(Ce6) was used as a control. The solution was added to a micro quartz cuvette with a

pathlength of 1 cm and a width of 1 mm (containing 0.5 mL solution), and then irradiated with a solid state laser beam at a wavelength of 660 nm (Xian Midriver Optoelectronics Technology, China).

2.3. Light-off cytotoxicity assay

The cellular viability after treatment with free Ce6 and DOX in DMSO, NPs and NPs(Ce6) in PBS was investigated against 4T1 cell lines using CCK-8 assays. Cells (5×10^3/mL) were plated in 96-well plates. Ce6 and DOX at different concentrations were added to the wells after 24 h, then the plates were incubated for another 24 h at 37 °C. At the same time, cells cultured in the complete medium without drugs were used as a control. After culturing cells for 48 h, the culture medium in each well was replaced by 100 μL 10% (*v*/*v*) CCK-8 solution. Additional 2 h incubation was applied and then the absorbance was read using a microplate reader (Biotek ELx800, Gene, USA). The cellular viability was measured by comparing with the control.

2.4. Light-on cytotoxicity assay

The effect of light intensity and illumination time on the cell viability was investigated by light-on cytotoxicity assays. The murine breast tumor cells (4T1) were treated with the NPs(Ce6) sample (Ce6 5×10^{-6} mol/L, DOX 1.34×10^{-5} mol/L) for 48 h and then each well was irradiated under a 660 nm laser source with light intensities ranging from 78 to 255 J/cm^2 for an illumination of time varied from 0 to 10 min. The cellular viability was assessed using the CCK-8 assay, which was operated in the same manner as the light-off group. 4T1 cells were also irradiated within a period of time from 0 to 10 min with a fixed intensity of 0.68 W/cm^2 in another assay. Each assay was performed in triplicate. Controls were the cells without incubation with NPs(Ce6) but irradiated at the same laser intensity.

2.5. Cellular uptake, ROS generation and PDT assay

The live cell imaging experiments were carried out *via* a confocal laser scanning microscope (CLSM) ZEISS 710. In order to study the intracellular localization of the nanoparticles, NPs(Ce6) (conjugated DOX 1.34×10^{-5} mol/L and Ce6 5×10^{-6} mol/L), NPs (conjugated DOX 1.34×10^{-5} mol/L), Ce6 (5×10^{-6} mol/L) and DOX (1.34×10^{-5} mol/L) in DMSO were incubated with 4T1 cells for 2 h. The intracellular DOX (Ex = 478 nm, Em = 556 nm) and Ce6 (Ex = 604 nm, Em = 675 nm) were observed under the CLSM after PBS wash.

The intracellular ROS level was quantified by fluorescence spectroscopy with 2′,7′-dichlorofluorescin diacetate (DCFH-DA) as a probe. 1×10^{-5} mol/L DCFH-DA was added into each well and then the plates were incubated at 37 °C in the dark. The cells were washed using PBS as washing buffer after 30 min incubation, and the fluorescence was captured with a microplate reader (Ex = 485 nm, Em = 535 nm).

The mechanisms for cellular uptake were investigated with endocytosis inhibitors. Cells were treated with 2×10^{-4} mol/L inhibitors including chlorpromazine, chloroquine, nocodazole, 2-deoxy-D-glucose, colchicine and NH_4Cl from Sigma Aldrich for 30 min, respectively. NPs(Ce6) (DOX 13.35 μmol/L, Ce6 5 μmol/L) were then incubated with cells. After 1 h incubation, cells were washed with PBS 3 times and then imaged under a confocal microscopy. All the image data were analyzed by LSM Image Browser and Image J.

2.6. Flow cytometry

Cellular apoptosis induced by NPs(Ce6) was investigated by flow cytometry. 4T1 cells were plated in 6-well plates at 1×10^6/well. The attached cells were treated with six formulations: complete media, complete media and laser irradiation for 5 min, NPs (DOX, 1.34×10^{-5} mol/L), NPs(Ce6) (DOX, 1.34×10^{-5} mol/L and Ce6, 5×10^{-6} mol/L), NPs(Ce6) (DOX, 1.34×10^{-5} mol/L and Ce6, 5×10^{-6} mol/L) and laser irradiation for 2 min, NPs(Ce6) (DOX, 1.34×10^{-5} mol/L and Ce6, 5×10^{-6} mol/L) and laser irradiation for 5 min. A laser source at a wavelength of 660 nm was applied in the assay. The plates were incubated for an additional 24 h and then detached and harvested as cell suspension. Annexin V: FITC and PI were added to the suspension in accordance with the manufacturer′s instructions, and the samples were analyzed by using a flow cytometer.

2.7. Fluorescence imaging study

To observe the potential biodistribution of nanoparticles in a 4T1 murine breast tumor model, 4T1 tumor cell suspension (0.1 mL, containing 5×10^5 cells) was injected into the right back of the female BALB/c mice (6−8 weeks old). When the tumor approximately reached 100 mm^3, mice were randomly divided into four groups (n = 3).

NPs(Ce6) (DOX, 4 mg/kg and Ce6, 5 mg/kg) and fluorescence-labeled NPs were applied to measure the targeting efficiency of the NPs, respectively. The *in vivo* fluorescent probe 1,1′-dioctadecyl-3,3,3′,3′-tetramethylindotricarbocyanine (DiR) (Ex = 748 nm, Em = 790 nm) was encapsulated into NPs by the film rehydration method[45]. Each sample was intravenously injected into mice (n = 3 per group) and the mice were sacrificed at pre-set intervals. Tumors and main organs, such as heart, liver, spleen, and lung, were excised and the fluorescence signal in these organs and tumors was detected by *In Vivo* Image System Fx Pro (Bruker, Germany).

2.8. Analysis of lysosomal escape and nuclear distribution of DOX

4T1 cells were treated with NPs(Ce6) (conjugated DOX, 1.34×10^{-5} mol/L and Ce6, 5×10^{-6} mol/L). After incubation for 8 h, a fresh medium was replaced and cells were washed with PBS 3 times. The cells were treated with or without light irradiation for 3 min under a 660 nm laser (200 mW/cm^2), and cells were further cultured for 2 h after light irradiation. The Hoechst 33342 (10 μg/mL) was used to stain cell nuclei, and LysoTracker green (0.5 μg/mL) to stain lysosomes. Lysosomal escape of DOX and Ce6 was observed using a CLSM. To observe nuclear distribution of DOX, cells were further cultured for 40 h after light irradiation, and the distribution of DOX was observed under a CLSM.

2.9. In vivo chemo-photodynamic therapy

Tumor-bearing mice models were developed in a similar way as described above. By the time the tumor reached 50−100 mm^3, all the mice were randomly divided into eight groups with seven animals per group. The administrated formula for each group were shown in Supporting Information Table S2. Tumors of the

irradiated groups were exposed under a laser beam with a wavelength of 660 nm (0.3 W/cm^2) for 30 min at 36 h post-injection, and 5 min off was applied for every 5 min laser irradiation. Each group was injected with the corresponding formulation by tail vein every 4 days 5 times. After administration, the tumor dimension and body weight were recorded every 2 days during 21 days. All these mice were sacrificed three weeks later. The major organs and tumors were excised and weighed. The tumor volume was calculated by the Eq. (1):

$$\text{Tumor volume} = \left(\text{Width}^2 \times \text{Length}\right) / 2 \quad (1)$$

The tumor growth inhibition (TGI) was calculated using the Eq. (2):

$$\text{TGI}\,(\%) = (W_0 - W_t) / W_t \times 100 \quad (2)$$

where W_0 and W_t represented the tumor weight of the PBS group and the treated group, respectively. The experiment protocol was reviewed and performed in compliance with Chinese guidelines for care and use of laboratory animals, and approved by the experimental animal ethics committee of the College of Pharmaceutical Sciences, Southwest University (No. 001563).

2.10. Statistical analysis

Results were analyzed by two-sided Student′s *t*-test for two groups and one-way analysis of variance (ANOVA) for multiple groups. Values of $^*P < 0.05$, $^{**}P < 0.01$ and $^{***}P < 0.001$ were considered to be statistically significant.

3. Results and discussion

3.1. Design, synthesis and characterization of the block polymeric prodrug

We employed the HPMA block copolymer to deliver therapeutic agents as it has been demonstrated as an efficient drug delivery carrier owing to its high water-solubility, great biocompatibility, and flexible chemical modification, and some of polyHPMA conjugates have entered into clinical trials[46]. The synthesis route for the amphiphilic and block polymeric prodrug, polyDOX-*block*-(polyHPMA-SS-polyHPMA)-*block*-polyDOX, was shown in Fig. 1 and Supporting Information S1. It has been accepted that the therapeutic indexes of polymeric DDSs are significantly affected by molecular structures, molecular weights (MWs) and compositions of polymeric carriers[47]. The EPR effect can be enhanced by optimization of the MW of the polymer, resulting in an improved tumor-targeting efficacy[48]. Previous studies from our group and other groups have shown that tumor accumulation of the HPMA polymeric prodrug can be boosted *via* increasing the MW up to 300 kDa[49,50]. However, as the backbone of the polyacrylamide-based polymer including the HPMA polymer is not biodegradable, or has a very slow degradation rate, the MW has to be controlled below 50 kDa so it can be cleared from the body *via* the kidney. We have prepared functional CTA with a disulfide linkage to mediate RAFT polymerization of the HPMA polymer (Supporting Information Scheme S1), resulting in a hydrophilic dimer polymer, polyHPMA-SS-polyHPMA. This polymer with a high MW (60−100 kDa) may have a prolonged blood circulation time and an enhanced tumor-targeting efficiency compared to traditional polymers with a MW below 50 kDa.

Additionally, a disulfide-functionalized monomer, MA-SS-DOX, was prepared. A dimer was used as a macroCTA to mediate RAFT polymerization of the hydrophobic monomer MA-SS-DOX, resulting in an amphiphilic and block polymeric prodrug. As the disulfide linkage was introduced to the backbone and the DOX was bonded to the polymeric carrier *via* the disulfide linker, the polymeric prodrug may be degraded and could release the drug in the tumor microenvironment owing to cleavage of the disulfide bond by GSH at a high intracellular concentration inside tumor cells. Meanwhile, the block and amphiphilic polymer could be used to encapsulate other agents, and therein it was used to load Ce6, a photosensitizer, to realize the combination of chemo-photodynamic therapy.

The molecule structure of CTA-SS-CTA, MA-SS-DOX and their intermediates were confirmed *via* ^{1}H NMR spectra, ^{13}C NMR spectra, LC-MS spectra, MAIDI-HR MS spectra (Supporting Information Figs. S1–S15). The synthesized polymers were analyzed by ^{1}H NMR spectra, UV−Vis spectrophotometry, and SEC analysis. Compared to the ^{1}H NMR spectra of the polymer polyHPMA-SS-polyHPMA (Fig. 2A), the proton peaks for the DOX-derivative were identified in ^{1}H NMR spectra of polyDOX-*block*-(polyHPMA-SS-polyHPMA)-*block*-polyDOX (Fig. 2B). UV−Vis spectra also confirmed DOX was successfully conjugated to the polymer, and the DOX content was 8.9% (*w*/*w*). After incubation with GSH, as shown in Supporting Information Table S3, the prodrug with a MW of 93.5 kDa (Fig. 2C) was degraded to products with a MW of 41.2 kDa (Fig. 2D), which was lower than that of the renal threshold limit (approximately 50 kDa).

Blank nanoparticles (NPs) were produced from the amphiphilic prodrug *via* the thin-film hydration method in PBS at pH 7.4, and nanoparticles NPs(Ce6) loaded with Ce6, a photosensitizer, were also prepared in the PBS solution. The critical micelle concentration (CMC) of the polymeric prodrug was characterized to be 0.014 mg/mL (Supporting Information Figs. S16 and S17). A low CMC value suggested the micelles could maintain their integrity under a highly diluted condition *in vivo*. The size distribution of NPs and NPs(Ce6) was characterized by DLS, and the average size of NPs and NPs(Ce6) was 60.3 ± 4.1 and 122.6 ± 5.5 nm, respectively (Fig. 2E). Structural stability of NPs was essential for *in vivo* body distribution and tumor accumulation. A characteristic absorbance peak of Ce6 at 660 nm was found in the UV–Vis spectrum of NPs(Ce6), and successful loading of Ce6 into nanoparticles was further evidenced by characteristic Ce6 emission spectra (Fig. 2F). The formation of NPs(Ce6) may be due to π–π stacking interactions between Ce6 and the DOX moiety as both agents had aromatic rings. In addition, a blue shift in the UV spectrum of NPs(Ce6) could be due to an increased polarity of the solution, which shortened the maximum absorption wavelength. A negative zeta potential of −7.54 ± 0.87 mV indicated that crown-shaped nanoparticles could be formed by the pHPMA block. Both NPs and NPs(Ce6) displayed a spherical morphology under a TEM and the average size for NPs and NPs(Ce6) was 25.5 ± 6.6 and 41.7 ± 9.4 nm, respectively (Fig. 2G and H). It was noted that different sizes were observed *via* DLS and TEM. The diameter obtained *via* DLS was a hydrodynamic one in a hydrated state. However, the diameter of the nanoparticles under a TEM was measured in a dehydrated state. This was in aligned with similar results of polymeric nanoscale DDSs obtained from other groups and our previous

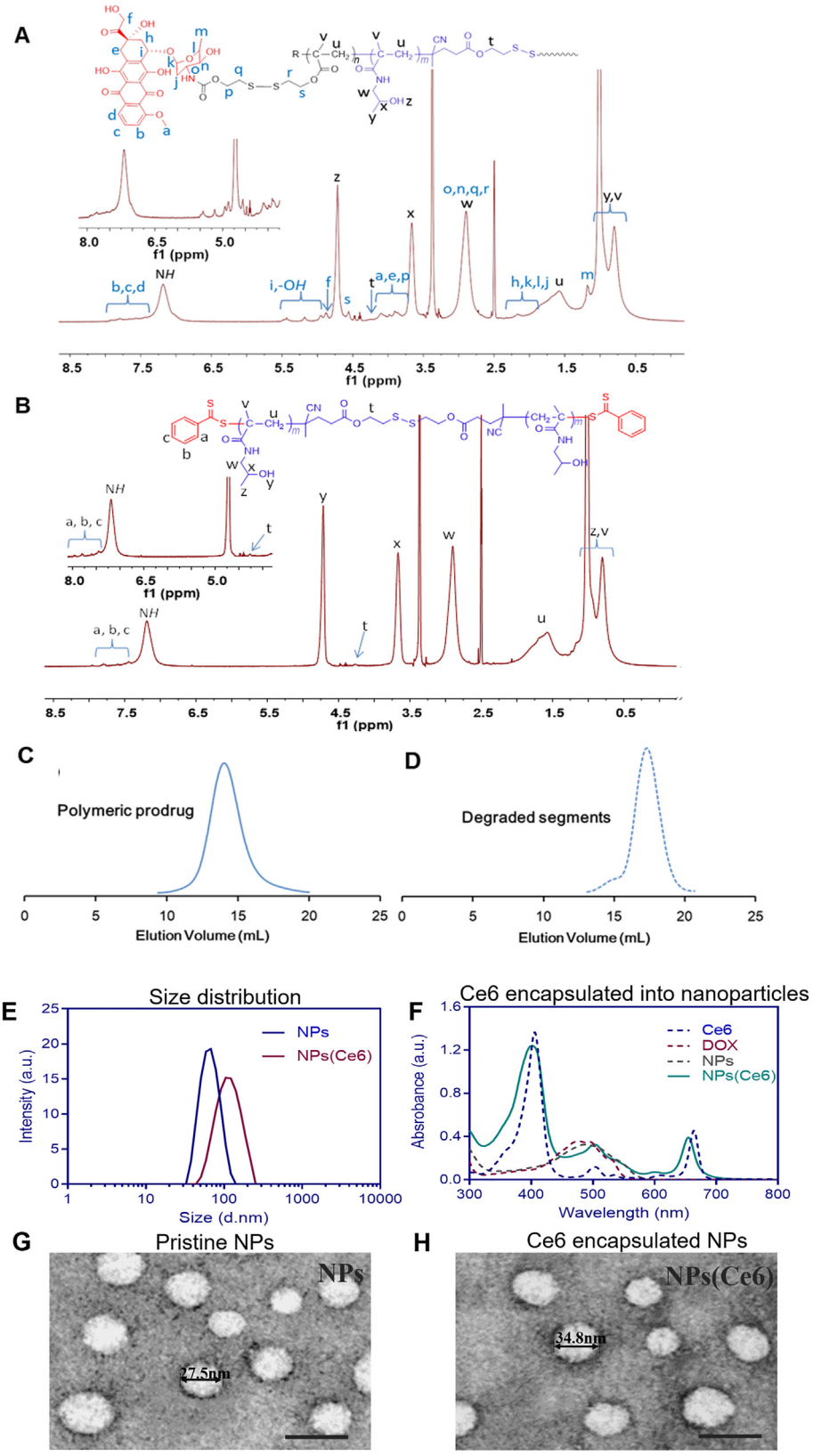

Figure 2 ^{1}H NMR spectrum of polyHPMA-SS-polyHPMA (recorded in d_6-DMSO) (A), and ^{1}H NMR spectra of the amphiphilic and block polymeric prodrug [polyDOX-*block*-(polyHPMA-SS-polyHPMA)-*block*-polyDOX] (solvent: d_6-DMSO) (B). Size exclusion chromatogram (SEC) of the final prodrug (MW 93.5 kDa) (C), and its degraded low-MW segments (MW 41.2 kDa) (D). Characterization of NPs and NPs(Ce6) with size distribution from DLS (E), UV–Vis absorption spectra (F); and TEM morphology of NPs (G) and NPs(Ce6) (H), scale bar: 50 nm.

studies[51]. The size and the zeta potential of NPs could be maintained in PBS and the DMEM medium for three days, although the particle size started to increase in the DMEM medium on Day 3 (Supporting Information Fig. S18).

3.2. *In vitro drug release*

Stimuli-responsive nanoparticles have been synthesized to allow rapid release of DOX after nanoparticles accumulated in the tumor cells. Since a much higher GSH level is found in tumor cells than normal cells, GSH could break the disulfide linker in NPs or NPs(Ce6) to release DOX. Both NPs and NPs(Ce6) were incubated in the media at a weakly acidic pH 5.4 and a physiological pH 7.4 with or without GSH that simulated the microenvironment in tumor tissues and normal tissues, respectively. As shown in Fig. 3, the release rates of both non-covalently encapsulated Ce6 and covalently conjugated DOX in NPs(Ce6) were remarkably higher in the medium with GSH. The cleavage of the disulfide linker by which the drug DOX was conjugated to the polymer carrier contributed to the released DOX in the GSH-containing medium. Another contributing factor was the degradability of the prodrug in the medium with GSH (Table S3) due to the reductive degradability of the disulfide linker in the polymer backbone. The balance between hydrophobic and hydrophilic moieties/segments was disturbed, which facilitated release of DOX and Ce6.

The release rate of DOX at both pH values with GSH was more than 70% at 36 h, while this rate was lower than 35% when GSH was absent (Fig. 3A). Simultaneously, more than 60% of Ce6 was released in the early 5 h in the medium with GSH, which was two times higher than that in the GSH-free medium (Fig. 3B). It was noted that the release rate of both covalently and noncovalently bonded drugs in NPs(Ce6) was not influenced by the pH values. Moreover, the release rate of non-covalently bonded Ce6 was faster than that of covalently bonded DOX, which indicated that the backbone of nanoparticles may be disintegrated to release Ce6 burstly before the majority of DOX molecules were sustainably released from the main chain of the polymer. The released drugs, including Ce6 and DOX, in pH 7.4 buffer solution containing 3 mmol/L GSH for 36 h were analyzed by RP-HPLC and ESI-MS. Abundant peaks (m/z = 569.25 and 542.10) were assigned as $[M+H]^+$ and $[M\text{-}H]^-$, which were correspondent to Ce6 and DOX (Supporting Information Fig. S19). The results suggested that the original structure of DOX detached from the polymer backbone cleaved by GSH was retained for its therapeutic efficacy.

3.3. *Cellular uptake, light-on/off cytotoxicity and in vitro PDT assay*

Different formulations were dosed to 4T1 murine breast cancer cells for 2 h and cells were observed under a CLSM to evaluate their cellular uptake. Both noncovalently encapsulated Ce6 and covalently bonded DOX were delivered into cells through the nanoparticles. The delivery efficiency *via* the nanoparticles was similar to that of free Ce6 due to free diffusion of Ce6 which was in a solution containing 0.5% *w/v* DMSO (Fig. 4, Left panel). The enhanced cellular uptake may be ascribed to trafficking the drugs-loaded nanoparticles through the cell membrane *via* endocytosis instead of free diffusion. The cell uptake mechanism of the nanoparticles was systematically investigated by inhibiting endocytosis pathways with different inhibitors. The fluorescence intensity drastically decreased in the NPs(Ce6)-containing cells suggested that clathrin-mediated endocytosis be dominant in the engulfment of NPs(Ce6) (Fig. 4, Right panel)[52].

3.4. *In vitro singlet oxygen ($^1O_2$) generation*

The encapsulated Ce6 was excited from an external light source to produce a key therapeutic component, strongly oxidative $^1O_2$. Anthracene-9,10-dipropionic acid disodium salt (ADPA) was employed to quantify $^1O_2$ production in PBS at pH 7.4 since ADPA can be specifically oxidized by $^1O_2$ and a decay in the peak height at 400 nm in the UV–Vis spectra provides a means of monitoring the $^1O_2$ production. After the NPs(Ce6) sample (Ce6 5.0 μmol/L, DOX 19.5 μmol/L) was mixed with ADPA (20 μmol/L), a decrease in the UV absorbance peak at 400 nm was observed after exposure to a 660 nm laser source (0.3 W/cm^2), however, the change in the ADPA absorbance peak at 400 nm was negligible in the absence of NPs(Ce6) (Fig. 5A and B). The results confirmed that laser irradiation activated NPs(Ce6) to generate $^1O_2$ from surrounding oxygen molecules.

Live cells incubated with NPs(Ce6) were scanned with a 660 nm laser 30 times every 10 s and monitored under a CLSM simultaneously. A ′bubbling′ phenomenon was observed both on the plasma membrane and intracellularly. This phenomenon was accompanied with an increase in the permeability of the cell membrane and outflow of the intracellular contents, which could induce apoptosis of peripheral cells and increase the anti-tumor immunogenicity. This was in agreement with the discovery that photodynamic therapy has subsequent anti-tumor immune effects after treatment[53]. The intracellular fluorescence intensity reduced

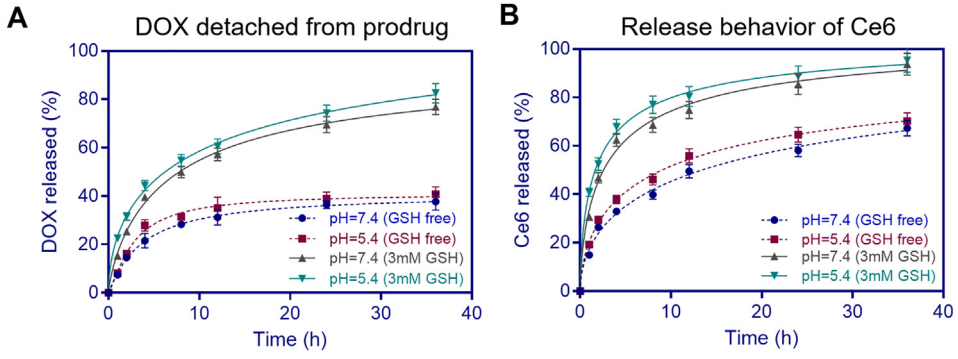

Figure 3 Cumulative release of DOX (a) and Ce6 (b) at pH 5.4 and 7.4 with/without 3 mmol/L GSH in the medium for 36 h (n = 3). mM, mmol/L.

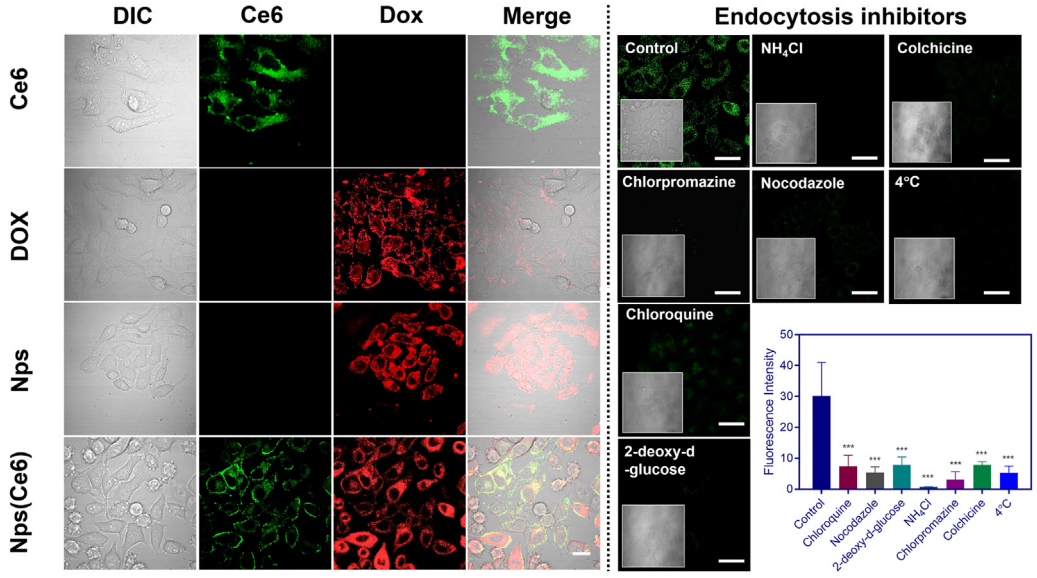

Figure 4 Uptake of NPs and NPs(Ce6) by 4T1 cells, scale bar: 20 μm (Ce6: Ex = 604 nm; DOX: Ex = 478 nm) on the left panel; Effects of different endocytic inhibitors and temperature (4 °C) on the cellular uptake of NPs(Ce6) on the right panel, scale bar: 40 μm, $n = 10$, data are expressed as mean ± SD, $^{***}P < 0.001$.

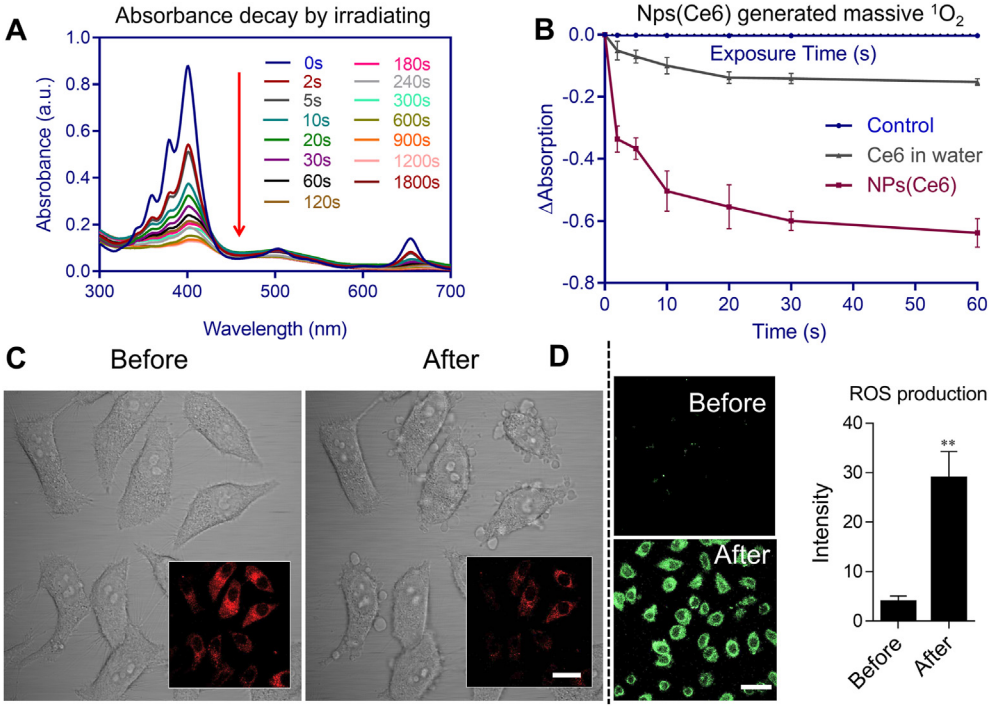

Figure 5 Singlet oxygen generation detected by a decay in the absorbance of ADPA after irradiation by a 660 nm laser for different durations (A); temporal changes in the ΔAbs of ADPA at 400 nm, $n = 3$, data are expressed as mean ± SD (B); Transmission images of NPs(Ce6)-treated cells before and after irradiation (C); Detection and quantification of the intracellular ROS level, data are expressed as mean ± SD (D). $n = 3$, scale bar = 40 μm, $^{**}P < 0.01$ *versus* the sample before the treatment using Student's *t*-test.

due to leakage of the cytoplasm contents out of cells after exposure to laser irradiation (Fig. 5C). Collapse of the cell morphology was associated with the intracellular ROS generation which was monitored using a ROS specific fluorescence marker, DCFH-DA. The cellular response to the oxidative stress was characterized with an enhanced signal intensity of green fluorescence after the cells were treated with NPs(Ce6) (Fig. 5D), indicating an increased level of ROS generated after cell were irradiated by a 660 nm laser.

3.5. *Cytotoxicity of NPs(Ce6)*

In order to study the cytotoxicity (chemotherapy) without photo-irradiation (light-off) and the cytotoxicity (chemo-photodynamic

combined therapy) with photoirradiation (light-on) of different formulations, CCK-8 assays were conducted after cells were dosed with these formulations with or without light exposure. The light-off cytotoxicity was investigated against both cancer (4T1) cells with a high GSH concentration and normal (HELF) cells with a low GSH concentration. Free Ce6 displayed negligible inhibition of cell growth (viability>100%) on 4T1 cells for a dose up to 20 μmol/L. The cytotoxicity of free DOX against 4T1 cells was much higher than free Ce6 with an IC_{50} of 1.4 ± 0.7 μg/mL, while conjugated DOX in NPs and NPs(Ce6) had a weaker cytotoxicity than free DOX and their IC_{50} values were 49.0 ± 5.2 and 40.5 ± 7.1 μg/mL (Supporting Information Fig. S20), respectively. However, the cell viability was around 30% by dosing with 10 μg/mL free DOX against HELF cells, while NPs and NPs(Ce6) did not inhibit cell growth even at the conjugated DOX concentration of 50 μg/mL, which indicated that the nanoparticles could reduce DOX toxicity to normal cells.

Furthermore, after cells were incubated with NPs(Ce6) for 48 h, cells were exposed to a continuous-wavelength 660 nm laser at various exposure intensities or durations. The cell viability dropped from approximately 70% to lower than 10% when the laser exposure intensity increased from 78 to 255 J/cm^2 at an exposure time of 5 min (Fig. 6A). Meanwhile, the cell viability decreased with a prolonged exposure time. The cell survival rate was around 25.1% after cells were exposed to the laser at an exposure intensity of 0.68 W/cm^2 for 10 min, while in the negative control group cells after a similar treatment maintained a viability of about 80.2% (Fig. 6B).

We also evaluated the effectiveness of the combinational treatment of chemo-photodynamic therapy in terms of tumor cell apoptosis by performing an Annexin V apoptosis detection assay with flow cytometry. Two dyes, Annexin V FITC and propidium iodide (PI), were used for identification of early and late apoptosis in the assay. The population of dead cells, late apoptosis (necrosis), early apoptosis and viable cells were represented by P2-Q1, P2-Q2, P2-Q3 and P2-Q4 in the results. The sum of P2-Q2 and P2-Q3 (Annexin V positive cells) refereed to the total apoptotic cell population. The apoptotic cells in the NPs(Ce6)-treated group increased with extension of the irradiation time (Fig. 6C). A large portion of apoptotic cells (around 44% and 55%) were found in NPs(Ce6)-treated group after exposure to light for 2 and 5 min, respectively. Apoptotic cells approximately doubled after treating cells with the combination of chemo-photodynamic therapy rather than NPs(Ce6)-alone treatment (Fig. 6D). The results demonstrated the feasibility and effectiveness of NPs(Ce6) for *in vitro* chemo-photodynamic combined therapy.

3.6. *Lysosome escape and nuclear distribution*

Intracellular ROS generated by the photosensitizer under light irradiation could promote drug release after rupturing lysosomal vesicles[54–56]. The distribution of NPs(Ce6) with or without light irradiation was investigated *via* a CLSM. The results showed that Ce6 in NPs destabilized lysosome membranes by generating ROS with light irradiation, leading to DOX escape from lysosomes evidenced with more red signals in the cytoplasm (Fig. 7A). To investigate the intracellular distribution of DOX, the nuclear location of DOX with and without NIR irradiation was examined (Fig. 7B). The DOX amount observed in the nuclei with NIR irradiation was evidently more than that without NIR irradiation, indicating nuclear translocation of DOX was enhanced by photosensitizer-mediated lysosomal escape.

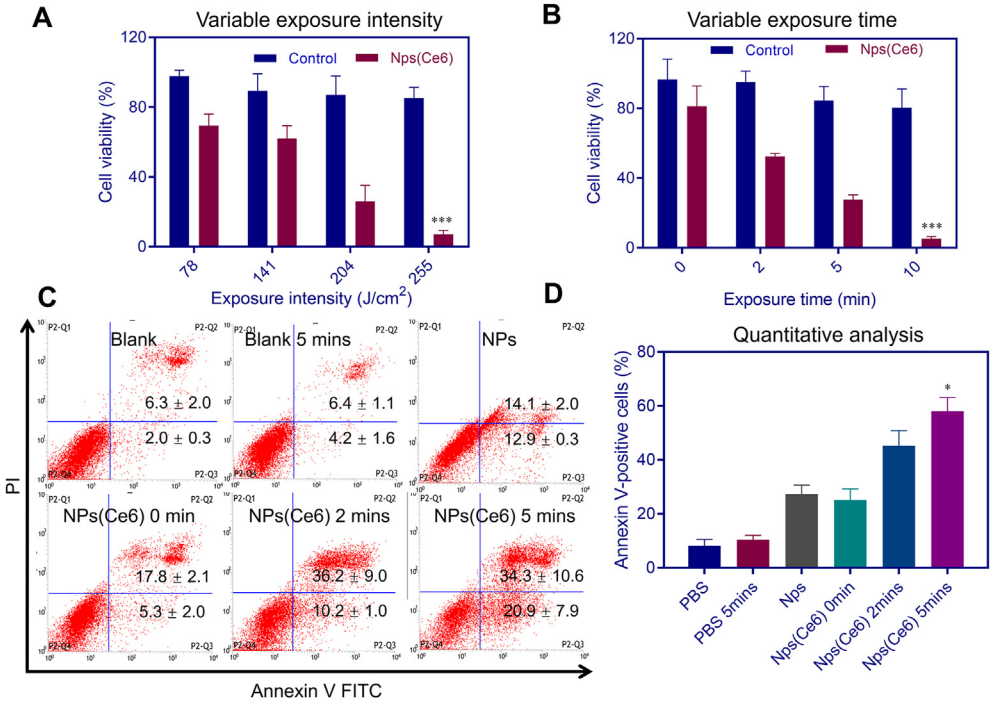

Figure 6 Cell viability with different irradiating intensities (A) and different exposure durations with a 660 nm laser (B). $n = 3$, $^{***}P < 0.001$ *versus* the blank control using Student's *t*-test. Annexin V-PI analysis of the synergistic apoptotic effect induced by NPs(Ce6) with irradiation *via* flow cytometry (C and D). $n = 3$, $^{*}P < 0.05$ *versus* the control in PBS using Student's *t*-test.

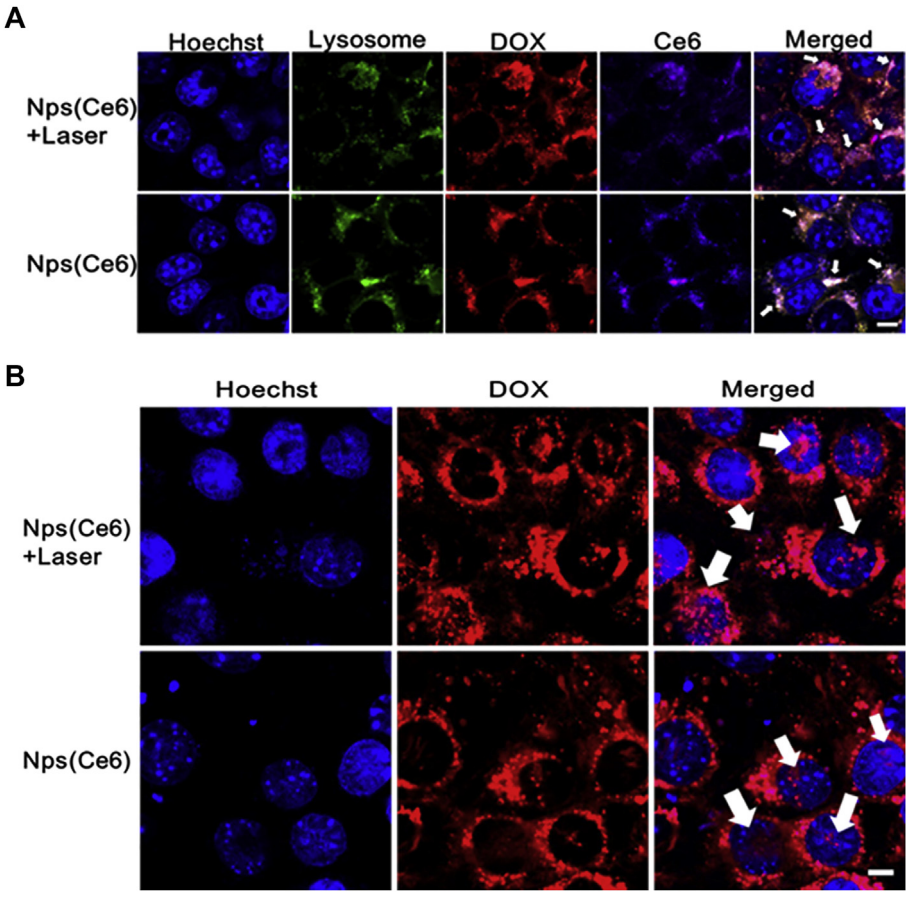

Figure 7 CLSM images of (A) lysosome escape and (B) nuclear distribution of NPs(Ce6) with or without light irradiation (scale bar: 10 μm).

3.7. Ex vivo imaging and in vivo anti-tumor efficacy

The *ex vivo* fluorescence was applied to analyze the distribution of NPs(Ce6) in different organs and provide a guidance for the starting time for PDT. A hydrophobic probe, DiR iodide, was encapsulated into the nanoparticles. The fluorescence signals in the tumor started to increase at 12 h and reached its maximum at 36 h post-injection. This fluorescence intensity slightly decreased after 48 h (Fig. 8A and B). The tumor-to-liver ratio (TLR) was calculated from the average *ex vivo* fluorescence intensities and the TLR data demonstrated efficient tumor accumulation of the nanoparticles instead of clearance by the liver (Fig. 8C). However, some of nanoparticles were distributed in the excised livers and spleens. This was due to the recognition of prodrug-based nanoparticles by the reticuloendothelial system. The nanoparticles could retain in the tumor, as the fluorescence signal could be observed for PDT at 36 h post-injection. This GSH-sensitive prodrug-based nanoparticles displayed great performance in both accumulating in tumor cells and targeting tumors.

To evaluate the *in vivo* anti-cancer efficacy of NPs(Ce6), 4T1 xenograft mice were administrated with NPs(Ce6) *via* tail vein (DOX dose: 4 mg/kg; Ce6 dose: 5 mg/kg). To obtain a PDT efficacy, a 660 nm laser beam (0.3 W/cm^2) was used to irradiate the tumors at 36 h post-injection. Mice were treated with the same procedure five times every 4 days. Compared to the PBS group, a slightly better anti-tumor effect was observed in mice treated with the laser alone, free DOX or free Ce6 ($P > 0.05$) (Fig. 8D). Both free DOX and free Ce6 may be rapidly cleared *in vivo*, thus only a very small amount of them reached the tumor site. Importantly, significant inhibition of the tumor growth was found in the NPs- or NPs(Ce6)-treated group, which may be attributed to efficient tumor accumulation of DOX and Ce6 in NPs or NPs(Ce6) *via* the EPR effect. The tumor growth inhibition (TGI) of NPs and NPs(Ce6) was 46.77% and 58.53%, respectively (Fig. 8E). It was notable that the chemo-photodynamic therapy with NPs(Ce6) showed a better efficacy than chemotherapy-alone treatment. The results suggested that DOX-mediated chemotherapy combined with Ce6-mediated PDT could significantly enhance the anti-tumor effect. The immunohistochemical staining analysis displayed effective inhibition of angiogenesis in the NPs(Ce6)-treated group compared to other groups by counting CD31 positive cells in the tumor tissue (Fig. 8F). A much higher percentage of TUNEL positive cells in the NPs(Ce6) treated groups with laser radiation suggested that the combinational therapy induced apoptosis of tumor cells more effectively. TUNEL's quantitative results were shown in Supporting Information Fig. S21.

Furthermore, no obvious changes in the body weight were detected after treatment with NPs(Ce6), indicating that chemo-photodynamic therapy had low or no systemic toxicity to mice (Supporting Information Fig. S22). After treatment of cells with NPs(Ce6) for 21 days, all mice were euthanized and sacrificed. The organs were analyzed by histological examination. H&E staining exhibited that there was no obvious damage observed in the heart treated with PBS, 660 nm laser, and different formulations. However, in the free DOX group, cardiotoxicity induced by DOX was observed evidenced with necrosis and infiltrated

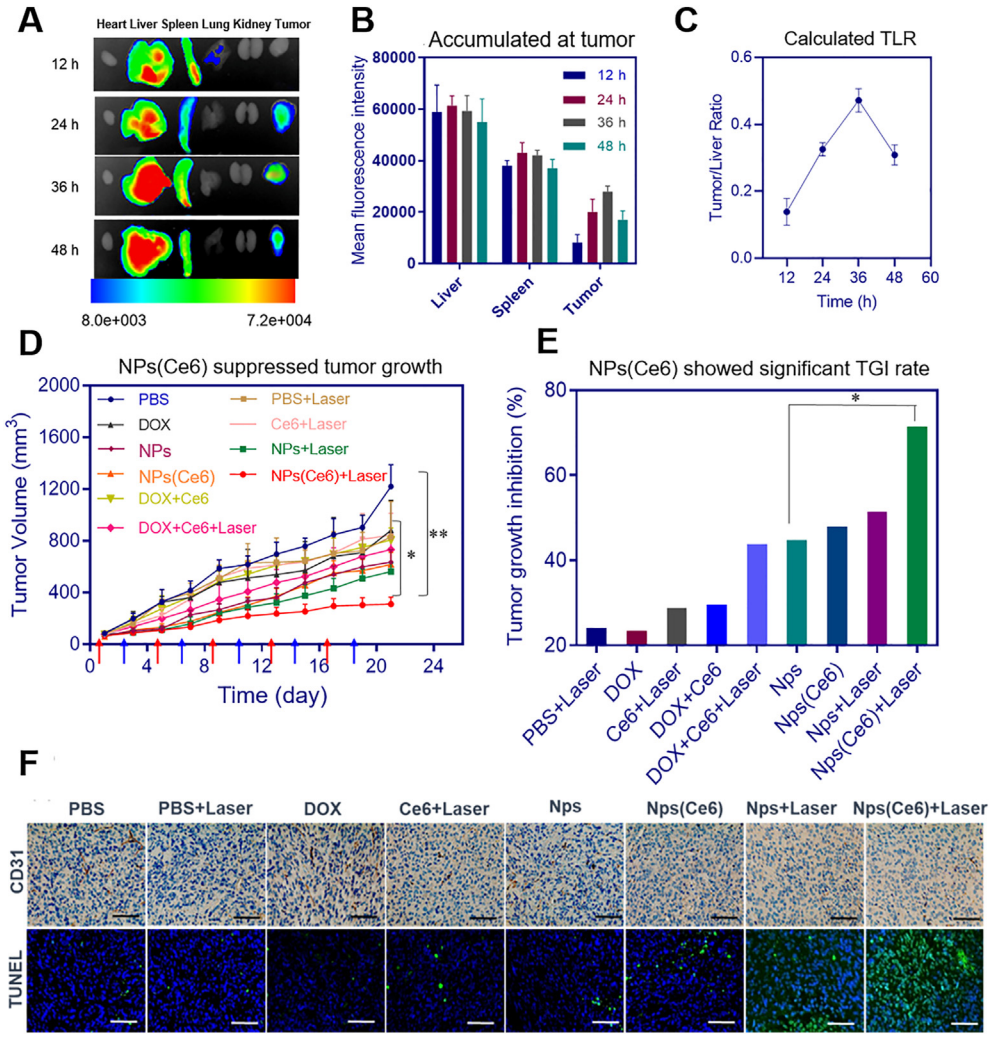

Figure 8 (A) *Ex vivo* distribution of NPs(Ce6) in organs and tumor for up to 48 h ($n = 5$); (B) Fluorescence signal intensity of NPs(Ce6) in tissues and tumors ($n = 5$); (C) Calculated distribution ratio TLR of NPs(Ce6) in the tumor to liver based on fluorescence intensities; (D) Tumor growth curves in mice bearing 4T1 tumor after treating with NPs(Ce6) with or without laser irradiation, red arrows indicated the time for injection of different formulations and blue for the time of laser administration (0.3 W/cm^2). $n = 7$, data are expressed as mean ± SD, $^*P < 0.05$ and $^{**}P < 0.01$ *versus* the DOX and PBS groups. (E) Tumor growth inhibition by the combinational therapeutic treatment method comparing to the chemotherapeutic group on Day 21 after first treatment; (F) CD31 and TUNEL staining of tumors (scale bar: 50 μm).

inflammatory cells (Supporting Information Fig. S23). It suggested that this delivery system could significantly reduce cardiotoxicity of DOX at the administration dose. In order to ensure the safety of the prodrug, we have also carried out blood biochemical index testing. The results (Supporting Information Fig. S24) showed that the drug had no obvious biological toxicity to mice at the experimental dose. In addition, we also conducted pharmacokinetic experiments to compare the *in vivo* efficacy of two formulations (DOX and NPs(Ce6)). The pharmacokinetic parameters were shown in Supporting Information Table S4. The results showed that at 36 h, since the GSH concentration in the blood was very low, only 35% of DOX was released from the drug carrier, indicating that NPs(Ce6) had good stability and the drug carrier could help reducing the systemic toxicity of DOX (Supporting Information Fig. S25). The significantly enhanced *in vivo* anticancer efficacy may be due to the combinational features of this drug delivery strategy: the GSH-sensitive polymeric prodrug was used as a carrier to deliver photosensitizers, resulting in its high accumulation in the tumor tissues, stimuli-responsive drug release behaviors and therefore a synergistically chemo-photodynamic anti-cancer efficacy.

4. Conclusions

The amphiphilic polymer-DOX prodrug was prepared *via* RAFT polymerization and photosensitizer Ce6 was encapsulated into the self-assembled nanoparticles. NPs(Ce6) could retain both drugs in a physiological condition and release both drugs by intracellular GSH. The nanosized NPs(Ce6) accumulated at the site-of-action after i.v. injection. This drug delivery system synergistically combined chemo and photodynamic therapy. The TGI of NPs(Ce6) reached 58.53% with an enhanced anti-cancer efficacy and negligible side effects. Photoirradiation at the tumor site promoted escape of the chemotherapeutic agent from lysosomes for a better efficacy. The fabricated polymeric prodrug-based

carriers have great potential against cancer as a combinational therapeutic system.

Acknowledgments

This research was financially supported by the National Natural Science Foundation of China (82073790, 51873120, 51673127, and 81621003), 1·3·5 project for disciplines of excellence, West China Hospital, Sichuan University, China (ZYJC21013, ZYGD18028).We are grateful to Sisi Wu, Xuemei Chen, Zhiqian Li, Hongying Chen, Yan Wang, Yanjing Zhang, Dingkui Pi, Fengfeng Chen, Jie Zhang, Yu Ding, Guonian Zhu and Yi Zhang (Core Facility of West China Hospital, Sichuan University, China) for their help *in vitro* and *in vivo* studies.

Author contributions

Kui Luo and Lei Luo designed the project. Lei Luo, Yiming Qi, Hong Zhong, Shinan Jiang and Kui Luo performed the experiments. Kui Luo provided experimental drugs and quality control. Lei Luo, Yiming Qi, Hong Zhong, Hu Zhang, Hao Cai, acquired, analyzed and interpreted the data. Lei Luo, Yiming Qi, Shinan Jiang and Hao Cai drafted the manuscript and Hu Zhang, Qiyong Gong, Zhongwei Gu and Kui Luo critically revised the manuscript. All of the authors have read and approved the final manuscript.

Conflicts of interest

The authors have no conflicts of interest to declare.

Appendix A. Supporting information

Supporting data to this article can be found online at https://doi.org/10.1016/j.apsb.2021.05.003.

References

1. Shi H, Sadler P. How promising is phototherapy for cancer.? *Br J Cancer* 2020;**123**:871−3.
2. Nam J, Son S, Park KS, Zou WP, Shea LD, Moon JJ. Cancer nanomedicine for combination cancer immunotherapy. *Nat Rev Mater* 2019;**4**:398−414.
3. Karges J, Kuang S, Maschietto F, Blacque O, Ciofini I, Chao H, et al. Rationally designed ruthenium complexes for 1-and 2-photon photodynamic therapy. *Nat Commun* 2020;**11**:3262.
4. Floyd JA, Galperin A, Ratner BD. Drug encapsulated polymeric microspheres for intracranial tumor therapy: a review of the literature. *Adv Drug Deliv Rev* 2015;**91**:23−37.
5. Li C, Wang JC, Wang YG, Gao HL, Wei G, Huang YZ, et al. Recent progress in drug delivery. *Acta Pharm Sin B* 2019;**9**:1145−62.
6. Senapati S, Mahanta AK, Kumar S, Maiti P. Controlled drug delivery vehicles for cancer treatment and their performance. *Signal Transduct Target Ther* 2018;**3**:1−19.
7. Wilhelm S, Tavares AJ, Dai Q, Ohta S, Audet J, Dvorak HF, et al. Analysis of nanoparticle delivery to tumours. *Nat Rev Mater* 2016;**1**:16014.
8. Brown TD, Whitehead KA, Mitragotri S. Materials for oral delivery of proteins and peptides. *Nat Rev Mater* 2020;**5**:127−48.
9. Anselmo AC, Gokarn Y, Mitragotri S. Non-invasive delivery strategies for biologics. *Nat Rev Drug Discov* 2019;**18**:19−40.
10. Xu C, Yu Y, Sun Y, Kong L, Yang C, Hu M, et al. Transformable nanoparticle-enabled synergistic elicitation and promotion of immunogenic cell death for triple-negative breast cancer immunotherapy. *Adv Funct Mater* 2019;**29**:1−20.
11. Rosenblum D, Joshi N, Tao W, Karp JM, Peer D. Progress and challenges towards targeted delivery of cancer therapeutics. *Nat Commun* 2018;**9**:1410.
12. Golombek SK, May JN, Theek B, Appold L, Drude N, Kiessling F, et al. Tumor targeting *via* EPR: strategies to enhance patient responses. *Adv Drug Deliv Rev* 2018;**130**:17−38.
13. Cai H, Xiang Y, Zeng Y, Li Z, Zheng X, Luo Q, et al. Cathepsin B-responsive and gadolinium-labeled branched glycopolymer-PTX conjugate-derived nanotheranostics for cancer treatment. *Acta Pharm Sin B* 2021;**11**:544−59.
14. Ojha T, Pathak V, Shi Y, Hennink WE, Moonen CTW, Storm G, et al. Pharmacological and physical vessel modulation strategies to improve EPR-mediated drug targeting to tumors. *Adv Drug Deliv Rev* 2017;**119**:44−60.
15. Cai H, Wang XJ, Zhang H, Sun L, Pan DY, Gong QY, et al. Enzyme-sensitive biodegradable and multifunctional polymeric conjugate as theranostic nanomedicine. *Appl Mater Today* 2018;**11**:207−18.
16. Deng H, Tan S, Gao X, Zou C, Xu C, Tu K, et al. *Cdk5* knocking out mediated by CRISPR-Cas9 genome editing for PD-L1 attenuation and enhanced antitumor immunity. *Acta Pharm Sin B* 2020;**10**:358−73.
17. Chen PM, Pan WY, Wu CY, Yeh CY, Korupalli C, Luo P-K, et al. Modulation of tumor microenvironment using a TLR-7/8 agonist-loaded nanoparticle system that exerts low-temperature hyperthermia and immunotherapy for *in situ* cancer vaccination. *Biomaterials* 2020;**230**:119629.
18. Zhang PH, Gao D, An KL, Shen Q, Wang C, Zhang YC, et al. A programmable polymer library that enables the construction of stimuli-responsive nanocarriers containing logic gates. *Nat Chem* 2020;**12**:381−90.
19. Gao C, Huang QX, Liu CH, Kwong CHT, Yue LD, Wan JB, et al. Treatment of atherosclerosis by macrophage-biomimetic nanoparticles *via* targeted pharmacotherapy and sequestration of proinflammatory cytokines. *Nat Commun* 2020;**11**:2622.
20. Dai JM, Luo Y, Nie D, Jin JH, Yang SL, Li G, et al. pH/photothermal dual-responsive drug delivery and synergistic chemo- photothermal therapy by novel porous carbon nanofibers. *Chem Eng J* 2020;**397**:1−11.
21. Hou X, Shou C, He M, Xu J, Cheng Y, Yuan Z, et al. A combination of LightOn gene expression system and tumor microenvironment-responsive nanoparticle delivery system for targeted breast cancer therapy. *Acta Pharm Sin B* 2020;**10**:1741−53.
22. Pan D, She W, Guo C, Luo K, Yi Q, Gu Z. PEGylated dendritic diaminocyclohexyl-platinum(II) conjugates as pH-responsive drug delivery vehicles with enhanced tumor accumulation and antitumor efficacy. *Biomaterials* 2014;**35**:10080−92.
23. Ekladious I, Colson YL, Grinstaff MW. Polymer−drug conjugate therapeutics: advances, insights and prospects. *Nat Rev Drug Discov* 2019;**18**:273−94.
24. Yang J, Wang T, Zhao L, Rajasekhar VK, Joshi S, Andreou C, et al. Gold/alpha-lactalbumin nanoprobes for the imaging and treatment of breast cancer. *Nat Biomed Eng* 2020;**4**:686−703.
25. Han X, Lu Y, Xie J, Zhang E, Zhu H, Du H, et al. Zwitterionic micelles efficiently deliver oral insulin without opening tight junctions. *Nat Nanotechnol* 2020;**15**:605−14.
26. Kopecek J, Yang J. Polymer nanomedicines. *Adv Drug Deliv Rev* 2020;**156**:40−64.
27. Zhang C, Yan L, Wang X, Zhu S, Chen C, Gu Z, et al. Progress, challenges, and future of nanomedicine. *Nano Today* 2020;**35**:101008.
28. Ekladious I, Colson YL, Grinstaff MW. Polymer−drug conjugate therapeutics: advances, insights and prospects. *Nat Rev Drug Discov* 2019;**18**:273−94.
29. Shi JJ, Kantoff PW, Wooster R, Farokhzad OC. Cancer nanomedicine: progress, challenges and opportunities. *Nat Rev Canc* 2017;**17**:20−37.
30. Zhang R, Luo K, Yang J, Sima M, Sun Y, Janat-Amsbury MM, et al. Synthesis and evaluation of a backbone biodegradable multiblock

HPMA copolymer nanocarrier for the systemic delivery of paclitaxel. *J Control Release* 2013;**166**:66−74.
31. Duan Z, Zhang Y, Zhu H, Sun L, Cai H, Li B, et al. Stimuli-sensitive biodegradable and amphiphilic block copolymer-gemcitabine conjugates self-assemble into a nanoscale vehicle for cancer therapy. *ACS Appl Mater Interfaces* 2017;**9**:3474−86.
32. Yang Y, Pan D, Luo K, Li L, Gu Z. Biodegradable and amphiphilic block copolymer-doxorubicin conjugate as polymeric nanoscale drug delivery vehicle for breast cancer therapy. *Biomaterials* 2013;**34**:8430−43.
33. He C, Duan X, Guo N, Chan C, Poon C, Weichselbaum RR, et al. Core-shell nanoscale coordination polymers combine chemotherapy and photodynamic therapy to potentiate checkpoint blockade cancer immunotherapy. *Nat Commun* 2016;**7**:12499.
34. Li D, Zhang M, Xu F, Chen Y, Chen B, Chang Y, et al. Biomimetic albumin-modified gold nanorods for photothermo-chemotherapy and macrophage polarization modulation. *Acta Pharm Sin B* 2018;**8**:74−84.
35. Lee H, Han J, Shin H, Han H, Na K, Kim H. Combination of chemotherapy and photodynamic therapy for cancer treatment with sonoporation effects. *J Control Release* 2018;**283**:190−9.
36. Xu S, Zhu X, Zhang C, Huang W, Zhou Y, Yan D. Oxygen and Pt(ll) self-generating conjugate for synergistic photo-chemo therapy of hypoxic tumor. *Nat Commun* 2018;**9**:2053.
37. Pei Q, Hu X, Zheng X, Liu S, Li Y, Jing X, et al. Light-activatable red blood cell membrane-camouflaged dimeric prodrug nanoparticles for synergistic photodynamic/chemotherapy. *ACS Nano* 2018;**12**:1630−41.
38. Huang C, Chu CC, Wang XY, Lin HR, Wang JQ, Zeng Y, et al. Ultra-high loading of sinoporphyrin sodium in ferritin for single-wave motivated photothermal and photodynamic co-therapy. *Biomater Sci* 2017;**5**:1512−6.
39. Wang T, Wang D, Yu H, Wang M, Liu J, Feng B, et al. Intracellularly acid-switchable multifunctional micelles for combinational photo/-chemotherapy of the drug-resistant tumor. *ACS Nano* 2016;**10**:3496−508.
40. Yu G, Yu S, Saha ML, Zhou J, Cook TR, Yung BC, et al. A discrete organoplatinum(II) metallacage as a multimodality theranostic platform for cancer photochemotherapy. *Nat Commun* 2018;**9**:4335.
41. Li W, Yang J, Luo L, Jiang M, Qin B, Yin H, et al. Targeting photodynamic and photothermal therapy to the endoplasmic reticulum enhances immunogenic cancer cell death. *Nat Commun* 2019;**10**:3349.
42. Luo L, Xu F, Peng H, Luo Y, Tian X, Battaglia G, et al. Stimuli-responsive polymeric prodrug-based nanomedicine delivering nifuroxazide and doxorubicin against primary breast cancer and pulmonary metastasis. *J Control Release* 2020;**318**:124−35.
43. Zhang C, Pan D, Luo K, Li N, Guo C, Zheng X, et al. Dendrimer-doxorubicin conjugate as enzyme-sensitive and polymeric nanoscale drug delivery vehicle for ovarian cancer therapy. *Polym Chem* 2014;**5**:5227−35.
44. Zhang C, Pan D, Luo K, She W, Guo C, Yang Y, et al. Peptide dendrimer-doxorubicin conjugate-based nanoparticles as an enzyme-responsive drug delivery system for cancer therapy. *Adv Healthcare Mat* 2014;**3**:1299−308.
45. Yu J, Wang Y, Zhou S, Li J, Wang J, Chi D, et al. Remote loading paclitaxel-doxorubicin prodrug into liposomes for cancer combination therapy. *Acta Pharm Sin B* 2020;**10**:1730−40.
46. Ferguson JP, Huber SD, Willy NM, Aygun E, Goker S, Atabey T, et al. Mechanoregulation of clathrin-mediated endocytosis. *J Cell Sci* 2017;**130**:3631−6.
47. Deng SH, Li XX, Liu S, Chen JF, Li MQ, Chew SYA, et al. Codelivery of CRISPR-Cas9 and chlorin e6 for spatially controlled tumor-specific gene editing with synergistic drug effects. *Sci Adv* 2020;**6**:eabb4005.
48. Li L, Yang Z, Zhu SJ, He LC, Fan WP, Tang W, et al. A rationally designed semiconducting polymer brush for NIR-II imaging-guided light-triggered remote control of CRISPR/Cas9 genome editing. *Adv Mater* 2019;**31**:1901187.
49. Shi LL, Wu WB, Duan YK, Xu L, Xu YY, Hou LD, et al. Light-induced self-escape of spherical nucleic acid from endo/lysosome for efficient non-cationic gene delivery. *Angew Chem Int Ed* 2020;**59**:19168−191774.
50. Xue XL, Qian CG, Fang HB, Liu HK, Yuan H, Guo ZJ, et al. Photoactivated lysosomal escape of a monofunctional Pt-II complex Pt-BDPA for nucleus access. *Angew Chem Int Ed* 2019;**58**:12661−6.
51. Wu Y, Li F, Zhang X, Li Z, Zhang Q, Wang W, et al. Tumor microenvironment-responsive PEGylated heparin-pyropheophorbide-a nanoconjugates for photodynamic therapy. *Carbohydr Polym* 2021;**255**:117490.
52. Yang J, Kopecek J. Macromolecular therapeutics. *J Control Release* 2014;**190**:288−303.
53. Zhou F, Feng B, Yu H, Wang D, Wang T, Ma Y, et al. Tumor microenvironment-activatable prodrug vesicles for nanoenabled cancer chemoimmunotherapy combining immunogenic cell death induction and CD47 blockade. *Adv Mater* 2019;**31**:180588.
54. Zhang X, Wu Y, Li Z, Wang W, Wu Y, Pan D, et al. Glycodendron/pyropheophorbide-a (Ppa)-functionalized hyaluronic acid as a nanosystem for tumor photodynamic therapy. *Carbohydr Polym* 2020;**247**:116749.
55. Kang H, Rho S, Stiles WR, Hu S, Baek Y, Hwang DW, et al. Size-dependent EPR effect of polymeric nanoparticles on tumor targeting. *Adv Healthc Mater* 2020;**9**:1901223.
56. Duangjai A, Luo K, Zhou Y, Yang J, Kopecek J. Combination cytotoxicity of backbone degradable HPMA copolymer gemcitabine and platinum conjugates toward human ovarian carcinoma cells. *Eur J Pharm Biopharm* 2014;**87**:187−96.